Combining E-ELT HIRES instrument and SKA to probe the chemical enrichment by the first stars

Katerina Stergiopoulou
Supervisor: Erik Zackrisson

Uppsala University, Department of Physics and Astronomy

April 27, 2016

Abstract

In this project we investigate the feasibility of detecting the signatures of Pop III stars in metal poor second generation stars and in gas clouds at high redshifts. First, the nucleosynthetic yields of Pair Instability Supernova and how they are manifested in gas clouds are presented. Next, some basic quantities of radio astronomy are explained and the requirements of SKA are shown. Then, the minimum detectable hydrogen column density of SKA for gas clouds at high redhsift is calculated and after that the basic principles of spectroscopy and the requirements of the HiReS instrument of E-ELT are demonstrated. Finally, suggestions about where the observations with HiReS should focus are made.

1 Introduction

The stars in the Milky Way were divided in to two categories, Population I and Population II stars, for the first time in 1944 by Walter Baade (1893-1960). Their classification was based initially on their location and on their orbit. Few years later the connection of star populations to metallicity was discovered by Nancy Roman.

Population I (Pop I) stars are considered metal-rich. The younger they are, the higher their metallicity. These stars are located in the disk and the youngest ones in the spiral arms of spiral galaxies. Their orbits lie on the galactic plane and they are almost circular. Population II (Pop II) are metal poor stars and older compared to the Pop I stars. Thus, they are low mass stars and redder. They are found in the galactic halo and in the galactic bulge. Their orbits pass through the galactic plane and they are highly eccentric[1].

In the late '70s, another star population started being used in publications. Population III stars are the first generation of stars and they have none or extremely low metallicity. They are thought to be very massive stars and they have not yet been confirmed observationally. By studying them we learn about the evolution of the first stars and how they contributed to the re-ionization and to the chemical enrichment of the early intergalactic medium (IGM). The first simulations about the formation of Pop III stars showed that these massive stars were formed iso-

lated, one per halo with masses $100M_{\odot} \lesssim M \lesssim 500M_{\odot}$. However, more recent simulations [3] showed how a substantial fraction of the very first stars formed in binary or even multiple systems with masses $40M_{\odot} \lesssim M \lesssim 500M_{\odot}$ [2][3]. On the other hand, simulations by Visby et al.[98] resulted in formation of even less massive Pop III stars, with the maximum mass of a Pop III star formed in a minihalo of $10^6 M_{\odot}$ being $\sim 50 M_{\odot}$.

2 Signatures of Pop III SNe in Second Generation (SG) Stars.

2.1 What should we look for?

Low mass SG stars are amongst the best objects to probe Pop III star formation and evolution, as they are the first metal enriched low mass stars with metals that come only from Pop III supernova (SN) explosions[4].

We are not sure exactly what chemical abundances to expect as Pop III signatures in SG stars, however we know some more general chemical patterns that would imply enrichment from Pop III SNe, such as Carbon Enhanced Metal Poor (CEMP) stars [5] and an odd-even effect which would indicate Pair Instability SNe (PISNe)[6]. These signatures may be difficult to find though, because besides PISNe, it is believed that Pop III stars with masses $15M_{\odot} < M < 40M_{\odot}$ were also formed and died as Core Collapse Supernova (CCSN)[6][7].

2.2 Pop III star formation

The formation of the first stars could occur in two kinds of environments which are determined from two corresponding cooling mechanisms of metal poor gas. Molecular hydrogen cooling triggers the star formation in minihaloes (MH)[8] and hydrogen line cooling leads to the formation of the first galaxies in atomic cooling haloes (ACH) [9].

It was thought due to early simulations that just one star was formed per MH with a characteristic mass $\sim 100M_{\odot}$ [10] and after the explosion the feedback was so strong that prevented further star formation [11]. However, recent simulations have shown that there are two mechanisms which can reduce the Pop III star masses: gravitational fragmentation in the disc that surrounds a Pop III protostar[12] and radiative suppression of protostellar accretion[43]. These mechanisms lead to the formation of multiple stars with lower masses $\geqslant 10M_{\odot}$ [12]. This is consistent with the α-element enhancements observed in metal poor stars which imply CCSN explosions[13].

In order to find Pop III star signatures we should investigate massive stars that exploded as PISN and spread the yields of nucleosynthesis into the early IGM. Assuming that the mass of a Pop III star in a MH is $\sim 100M_{\odot}$[10], no other stars would be able to form in the particular MH, after the death of the star as a PISN[4].

ACH were already polluted with metals before their virialization, thus we can assume than Pop III stars were not formed there. However, the estimation of the number of MHs that merged into an ACH is possible[15].

The lack of low mass Pop III stars in MW and in nearby galaxies suggests a mass limit of $0.8 M_{\odot}$ for the formation of the first stars[42][44]. Additional characteristics which distinguish Pop III stars from metal enriched stars are that the former can be rapid rotators[45] and that they show increased ionizing flux due to their high surface temperatures[46].

2.3 Pair Instability Supernovae (PISNe)

The first models of Pop III star formation showed that they were massive stars: $100 - 500 M_{\odot}$. They formed one per dark matter halo ($10^5 - 10^6 M_{\odot}$) at redshifts $z \sim 20-30$. However, as it has been already mentioned, recent models have shown that there is a fragmentation of the protostellar disc which leads to multiple Pop III star systems, with less massive objects though. The result is that a great number of these stars have died as CCSN ($15 - 40 M_{\odot}$) and they did not leave a signature that would distinguish them from Pop II and Pop I CCSNe. Only stars with an initial mass between $140 - 260 M_{\odot}$ or rapid rotators

with a lower limit mass of $80M_\odot$ explode as PISN, the most massive ones of which release energy up to 10^{53}erg[73].

The nucleosynthetic yields of PISNe depend on the mass of the progenitor stars. Heger & Woosley 2002[6] ran a series of simulations (non-rotating Pop III stars) to find how the yields depend on the He core mass. The He core mass varied between the limits $60M_\odot < M_{\rm He} < 140M_\odot$ while all the progenitor Pop III stars have the same mass $200M_\odot$ ($93M_\odot$ He core). The odd-even effect that we expect to detect in gas clouds depends on the neutron excess at the moment the He burning starts. For their simulations they used the value $\eta = 1.9 \times 10^{-7}$, whereas for stars with metallicity similar to the Sun its value is approximately 0.002. This low value of η is the result of low CNO abundances in Pop III stars[6].

The stars that exploded as PISNe had He cores with masses $64M_\odot < M_{\rm He} < 133M_\odot$ from which they inferred the initial stellar masses to be $140M_\odot < M < 260M_\odot$. The result of the low value of neutron excess is that isotopes such as ^{56}Fe,^{48} Ti,^{52} Cr,^{60} Ni were formed in high abundances, whereas isotopes that need high excess of neutrons (isotopes with odd charge) such as ^{14}N,^{23} Na,^{27} Al,^{31} P and (neutron rich isotopes) ^{29}Si,^{30} Si,^{33} S,^{34} S,^{36} S,^{38} Ar etc. were formed in small quantities. Additionally, there is no production of elements above the iron peak ones, because s- and r- processes did not take place again due to the deficiency of neutrons[6].

2.4 SG stars

Metal poor stars show metallicities of the order of $Z \sim 10^{-4}(10^{-5}[4])Z_\odot$. Pop II SG stars were formed both in MH and in ACH unlike the Pop III stars. In the MH case, star formation of Pop II stars occurs when the SN feedback is weak[16]. These SG stars were formed out of a mix of ejecta and pristine gas[17]. The virialization of MHs happened at redshift $z \sim 25$ and of ACHs at redshift $z \sim 10$ and their approximate masses are $10^6 M_\odot$ and $10^8 M_\odot$ respectively[18][19]. In ACHs the star formation of SG stars is triggered by atomic line cooling approximately at the virialization time $z \sim 10$[4]. When SG stars are formed in a MH, it means that the SN feedback was not that strong, thus the progenitor star was of lower mass and possibly multiple lower mass Pop III were formed in that MH, the yields of which contributed to the gas forming the SG star. In addition, the gas from which SG stars were formed in ACH was already metal enriched from the merging MHs, hence in both cases (MHs and ACHs) the formed SG stars contain enriched gas from several SNe and not just from one[4].

2.5 Chemical Signatures

Unique chemical abundances of CEMP and PISNe would be easier to detect in SG stars in comparison to detecting Pop III CCSNe yields, considering that the latter show similar signatures to high metallicity CCSNe [24].

Assuming that the enhanced carbon abundance in metal poor stars was caused by Pop III SNe, although it has not yet been confirmed that it can not be caused by other non primordial processes[25], there are two mechanisms which lead to CEMP yields, namely removing iron and adding carbon. The iron removing mechanism could be the mixing and the fallback of faint CCSNe[26], while the carbon adding mechanism could be the winds of fast rotating Pop III stars[27]. An approximate limit to the carbon abundance relative to iron could be set, [C/Fe] > 0.7[4][28] or [C/Fe] $> +0.1$, while Fe/H < -1.0[42]. As the metallicity decreases the fraction of stars that are CEMP increases[47].

However, there has been observed a dichotomy of the metal poor stars namely the carbon enhanced metal poor stars and the carbon normal metal poor stars[13]. A possible explanation could be that there are two classes of SNe with different explosion recovery times (the time that is required after the explosion for the appearance of cold gas and the beginning of SG star formation) and different energies[51], with the more energetic explosions $E_{SN} > 10^{51}$erg to be the ones with the longer recovery times and normal carbon abundances[54]. Thus, the CEMP stars may be the result of weaker explosions with more rapid recoveries[51].

Table 1: Nucleosynthetic Signatures of CEMP[4].

	CCSN[20]	Faint SN[21]	Wind+SN[22]	Pop II SN[23]
Mass ($M_\odot$)	20	20	20	20
E_{SN} (10^{51}erg)	1	0.74	1	1
C ($M_\odot$)	0.211	0.20	1.034	0.128
Fe ($M_\odot$)	0.072	1.09×10^{-5}	0.072	0.073

PISNe show an odd-even effect in their yields that may be detected. A typical ratio of an odd and even element, Co and Ni respectively, could be [Co/Ni] < −0.5[4].

Two emerging questions about the feasibility of the detection of the aforementioned signatures are if SG stars can preserve these chemical abundances and for how long. An attempt for these questions to be answered is through metal enrichment models[4], which have shown that the chemical signatures of Pop III stars can be preserved in SG stars even though the gas from which they formed had been enriched from several Pop III SNe. These simulations also showed that after the explosion of the first Pop II SNe, the Pop III signatures disappear. If we want to search for individual stars in MW and in nearby galaxies, we should consider any star with metallicity [Fe/H] < −4 and unique abundances as possible SG star[4]. On the other hand, a simulation of a single and not multiple Pop III SNe has shown that the unique signatures of a SN explosion may not be preserved in star forming clouds assuming inhomogeneity and anisotropy of the ejecta[42].

SG stars may be easier to be found in dwarf galaxies[30]. More specifically, star formation history in MW's ultra faint dwarfs shows that star formation took place for a short period of time and consequently the majority of their stars are expected to be SG stars[31].

On the other hand, PISN signatures may be much more difficult to be detected since the strong odd-even effect that indicates their existence is quickly erased by Pop II CCSNe. What is more, PISN signatures would be observed in stars with higher metallicities due to large Ca yields of them. Thus, they would not appear in searches which are based on the weak Ca II K line [14]. Another feature of PISNe is that their ejecta are dispersed in greater volumes than CCSNe ($R \sim$ 1kpc) making it difficult to form SG stars since the gas is not confined in a small volume. Thus, it may be easier to detect PISN signatures using absorption spectroscopy at the IGM gas at high redshifts. The metal enrichment of the diffuse IGM just by two PISNe will result in metallicity $Z = 10^{-4} Z_\odot$ [29].

In general though, there are uncertainties considering the Pop III SN yields because of their dependence on the progenitor mass, rotation rate, the presence of a companion, the initial metal abundance and also possible uncertainties due their sensitivity to instabilities before and during the explosion [3][6][49]. Thus the aim is to reverse engineer the observed abundances to find details about the nucleosynthesis of the first stars[48][50].

Table 2: Nucleosynthetic Signatures of PISN[4].

	CCSN[20]	PISN[6]	Pop II SN[23]
Prog. Mass ($M_\odot$)	20	195	20
E_{SN} (10^{51}erg)	1	40	1
C ($M_\odot$)	0.211	4.13	0.128
Na ($M_\odot$)	0.0029	0.00028	0.00181
Mg ($M_\odot$)	0.150	4.39	0.247
Ca ($M_\odot$)	0.00623	0.993	0.00921
Fe ($M_\odot$)	0.072	3.08	0.073
Co ($M_\odot$)	1.5×10^{-4}	5.59×10^{-6}	6.21×10^{-5}
Ni ($M_\odot$)	0.00175	0.00825	7.11×10^{-4}

3 Metal poor damped Lyman alpha systems

3.1 Dwarf Galaxies

Dwarf Galaxies are the most common galaxies, they are usually metal poor and they can be found in low and high redshifts[33][39]. Considering that the star formation in a large fraction of dwarf galaxies took place between redshifts $z \sim 1 - 4$ [34], we should be able to see the pre-existing cold neutral hydrogen clouds. These clouds would appear as damped Lyman alpha systems (DLAs)[39], with a hydrogen column density of N(HI) $\geqslant 10^{20.3}$ [35] and a metallicity at z ∼ 3 of Z ∼ $1/30 Z_\odot$[36]. The lowest metallicity of such a system found is [Fe/H] = −3.45[37]. We might even find systems that have only been enriched by just one generation of Pop III SNe[38]. Observation data that links the dwarf galaxies of the local group and high redshift VMP DLAs is that DLAs

with metallicities [Fe/H] $\leqslant -2.0$ show an enhancement in their α/Fe ratio that agrees with observations of nearby galaxies as well as of metal-poor MW halo stars showing that VMP DLAs may be the progenitors of dwarf galaxies[39].

3.2 Lyman Alpha Forest

The Lyman Alpha Forest appears when clouds of hydrogen in the IGM are located in the line of sight in front of a bright source such as a quasar (or a galaxy). As the light of the source passes through the gas, a 'forest' of absorption lines is shaped and added on the continuum quasar spectrum. Systems with column densities greater than $10^{14.5}\mathrm{cm}^{-2}$ show besides the hydrogen absorption lines and metal ones. Lyman limit systems, which are clouds with column densities N $\geqslant 10^{17}\mathrm{cm}^{-2}$, show, due to their denser nature, a break at the limit of Lyman series[92].

There was a lower limit until recently, set by observations, of metallicity at high redshift universe of approximately Z $\sim 10^{-3}\mathrm{Z}_{\odot}$ (whereas for individual stars the limit is close to $\sim 10^{-4}Z_{\odot}$). Simulations, consistent with the observations, have shown that the enrichment from Pop III SNe can increase the metalicity of the ISM in a MH up to Z $\sim 10^{-3}\mathrm{Z}_{\odot}$ and enrich also the IGM of the early universe (z $\sim$ 6)[52]. However, Fumagalli et al. 2011[52] discovered two (double) Lyman Limit Systems at redshifts $z \sim 3.4$ and $z \sim 3.2$ with no detectable metal absorption lines. They modelled the hydrogen lines to find upper limits for the column densities of various metals and the metallicity of the gas. Their results for the metallicities of the two systems were $Z_1 < 10^{-4.2}Z_{\odot}$ and $Z_2 < 10^{-3.8}Z_{\odot}$. This means that there are parts in the universe with almost pristine gas (very low chemical enrichment) for redshifts $z < 6$[52].

Table 3: Column density limits for Lyman alpha systems.

Lyman System	Column Density (cm^{-2})
Lyman Alpha Forest (with metal lines)	$> 10^{14.5}$
Lyman Limit System	$> 10^{17}$
Damped Lyman Alpha System	$> 10^{20.3}$

3.3 Metal poor DLAs

Hydrogen gas clouds with column densities N(HI) $\geqslant 10^{20.3}\mathrm{cm}^{-2}$[35] are so dense that they are shielded against ionizing radiation and thus they are mainly neutral[92]. These clouds are called Damped Lyman systems because their lines are broadened (damping wings) and they are studied for redshifts up to $\sim$ 5[92].

The usual way to measure the ratio [α/Fe] in metal poor DLAs (Z $< 1/100\mathrm{Z}_{\odot}$) is by tracing Si II (representative of α elements) and Fe II (representative of Fe-peak elements)[39]. A further step would be the comparison to Galactic halo star ratios using at this case an average of [Mg/Fe], [Si/Fe] and [Ca/Fe][39]. The comparison of observational data[39][40][41] shows that there are many similarities concerning chemical evolution between the dSph of MW and DLAs at redshift $z \sim 2-3$[39].

There are parameters than can be directly measured from the obtained spectral lines of DLAs, such as the column density of neutral hydrogen, chemical composition, temperature and turbulence (by decoupling of thermal and turbulent line broadening)[39]. Depending on redshift, metallicity, column density and blending it is common one or more of the ratios NII/NI AlIII/AlII SiIII/SiII FeIII/FeII to be measured. The SiIII/SiII ratio appears to be strongly dependent on the column density of hydrogen. Using these ratios and the mass, density can be calculated as well as the size of the cloud. Other quantities that can be inferred by making some geometry assumptions are the total mass of the neutral gas, the thermal and turbulent gas pressures, the sound speed of gas and the turbulent Mach number[39].

The values of the aforementioned quantities show some patterns for metal poor DLAs. The more metal poor a DLA system is the more the probabilities of detecting signatures of Pop III enrichment[39]. Hydrogen in DLAs is mostly neutral and this ensures the accuracy of the abundance measurements. The majority of the metals are singly ionized (e.g. FeII, SiII), with their ionization potential being lower than the hydrogen one (13.6eV). However, some elements appear neutral (e.g. OI, NI)[94]. In a metal poor DLA, carbon abundance is difficult to be measured

and only some limits can be set for the oxygen abundance. On the other hand, it is easier to measure the abundances of Fe, Si and S[94].

The equivalent width of a damped Lyman alpha line with respect to the column density is given by the relation[94]:

$$W \sim 10\left[\frac{\mathrm{N(HI)}}{2\times 10^{20}\mathrm{cm}^{-2}}\right]^{1/2} \text{Å} \qquad (1)$$

Assuming that the minimum column density of the DLAs we investigate is $\mathrm{N(HI)} \sim 2\times 10^{20}\mathrm{cm}^{-2}$, the minimum equivalent width (at rest) is $W_{\mathrm{min}} = 10$Å and the minimum observed one for redshift z=3 would be $W_{\mathrm{obs}} = 40$Å. These lines are considered strong and are distinguishable from a Lyman forest line since the equivalent width of the latter is approximately 3Å[94].

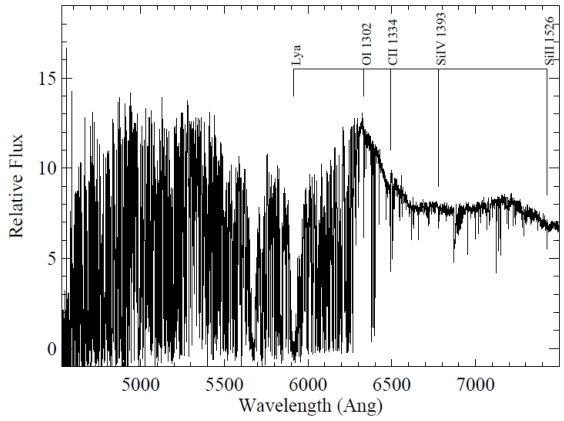

Figure 1: Spectrum of QSO PSS0209+0517 (Keck/ESI)
Image credit :[94]

In Fig.1 (Wolfe et al. 2005[94]), there is the spectrum of the quasar QSO PSS0209+0517. We can see the Lyman alpha forest, metal lines and two DLAs for redshifts z=3.864 and z=3.667. Wolfe et al. [94] showed that there is a lower limit for the metallicity of DLAs $Z > -2.6$ whereas the analysis of Lyman alpha forest instead [95] has shown lower metallicities. For example, Simcoe R. et al. 2003 [96], by analysing spectra of quasars, found that in the IGM at redshift $z \sim 2.5$ the 30% of the lines of Lyman alpha forest show abundances $[[\mathrm{C,O/H}]] \leqslant -3.5$[96].

4 Low Ionization Metal Absorbers

When we look for Pop III signatures, it is obvious that the possibility to find systems which are not polluted by Pop II CCSNe is greater for higher redshifts. There are three types of absorbers namely highly ionized systems (C IV, Si IV), low ionization systems (OI, CII, SiII, FeII) and MgII systems. The detection of low ionization absorbers is a way to investigate the high redshift Universe and trace neutral hydrogen[88].

Finding low ionization metal absorbers in gas clouds where neutral hydrogen dominates (located at our line of sight in front of a quasar) at redshift $z \geqslant 6$ first, and then measuring the abundances of the these metals, will show us after a comparison with the expected values, if a particular cloud/halo hosted Pop III stars without being polluted by other types of SN. Some of the low ionization absorption lines that can be observed are OI ($\lambda = 1302$Å), Si II ($\lambda = 1260$Å, $\lambda = 1304$Å) and CII ($\lambda = 1334$Å)[87]. The abundance of OI in a cloud can be inferred from the equivalent width and the column density since the absorption lines at $z = 6$ are not saturated like they are at lower redshifts[88].

5 Radio Astronomy

5.1 Measurements in Radio waves

The atmosphere of the Earth allows not only optical wavelengths to reach the surface of the Earth but also radio waves, giving the astronomers the opportunity to observe the universe with Earth based telescopes in another part of the electromagnetic spectrum. The radio window spreads to wavelengths approximately between 1 mm and 100 m. Shorter and longer wavelengths are absorbed by the atmosphere and the ionosphere of the Earth respectively. Thus, in order to cover the whole range of radio waves, telescopes with different operational requirements are needed, unlike the optical spectrum which can be covered by one telescope[71].

With radio-telescopes we can observe the solar system, distant objects with very low temperatures with their thermal radiation being in radio-waves and objects that emit synchrotron radiation. Radio galaxies, pulsars, the centre of the Milky Way, supernova remnants, ionized hydrogen and neutral hydrogen clouds in the ISM and IGM and molecular clouds are some interesting objects that are being investigated by radio astronomers[71].

Neutral hydrogen clouds can be detected in radio waves by observing the absorption line at 21.1 cm (1420.4 MHz) due to the hyperfine structure of the ground state of hydrogen. The advantage of these observations in radio waves is that they are not absorbed by interstellar dust as the optical waves are[71].

A very useful technique that is used in Radio Astronomy is Interferometry. Large numbers of antennas which can be connected by optical fibres are combined and this array of antennas functions as a single huge telescope. The sensitivity to weak signals depends on the effective collecting area and thus on the number of antennas. What is more, better resolution is achieved when the antennas are distributed over long distances because it depends on the separation of the individual receivers and not on their diameter[72].

5.2 Square Kilometer Array (SKA)

The Square Kilometer Array is an international project the goal of which is to build the largest radio interferometer yet, with an enormous collecting area, greater than 1 km^2, which will consist of numerous antennas, up to three thousand parabolic ones with a 15 meter diameter each (SKA mid) and up to one quarter of a million dipoles (SKA low), distributed over a few thousand kilometers mainly in South Africa and in Australia respectively. It will investigate the evolution of the early universe since it will be powerful enough to detect faint signals at high redshifts, as well as the fundamentals laws of physics such as the theory of relativity and the nature of dark matter and energy[72][74][84].

The construction of the sites and telescopes will start in 2018 and it will take place in two phases: Phase 1-SKA1 and Phase 2-SKA2. Phase 1 will consist of three components namely a low frequency aperture array (SKA1 low), a mid frequency dish array (SKA1 mid) and a mid frequency survey array (SKA1 survey). The frequency range of SKA1 mid will be 350 MHz – 13.8 GHz and of SKA1 low 50 MHz – 350 MHz. After the completion of the first phase SKA will have reached 15-20% of its capabilities. SKA1 low will have a collecting area of 0.4 km^2 and it will consist of 130,000 dipoles grouped into approximately 512 stations, while the SKA1 mid will consist of a 150-km array with a collecting area of 33,000 m^2 which will be the result of 133 15-m diameter SKA1 mid dishes and 64 13.5-m diameter dishes from the MeerKAT telescope[72][76][85][86].

SKA low will focus mainly on the Epoch of the re-ionization, thus the observations will begin at redshift z=6 and reach redshifts greater that 15. That means that the required frequencies to map the neutral hydrogen of the universe during the Epoch of Reionization are lower than 200MHz and the goal is frequencies lower than 89MHz[74]. In the tables 4 and 5, the scientific and technical requirements for investigating the re-ionization epoch (EoR) by studying the neutral IGM and the 21cm forest are shown, and in table 6 the specifications of SKA mid design can be seen.

Table 4: SKA low requiremetns for probing the neutral IGM during the EoR[81].

Parameter	Value
Reshift	6-30
Angular resolution	1 arcmin
Radial resolution	0.1 Mpc
FoV	5deg^2
Frequency range	50-200 MHz
Frequency resolution	10 kHz
Maximum Baseline	> 5km

Table 5: SKA low requiremetns for probing the EoR using the 21cm forest[81].

Parameter	Value
Reshift	6-20
Optical depth	0.001
Velocity resolution	0.2 km/s
Frequency range	70-200 MHz
Frequency resolution	0.1 kHz

Table 6: SKA mid design specifications [74].

Parameter	Value
Frequency range	0.3-10 GHz
Sensitivity ($A_{\mathrm{eff}/T_{\mathrm{sys}}}$)	0.23 Jy ($1.2\times10^{4}\mathrm{m^2K^{-1}}$) at 1.4 GHz
Survey speed	$6\times10^{7}\mathrm{deg^2m^4K^{-2}}$ at 1.4 GHz
Antenna diameter	15 m
Number of antennas	3000
System temperature	30 K

5.2.1 SEFD of SKA1 low

The System Equivalent Flux Density (SEFD) is a measure of an antenna's sensitivity and is given by the following formula[75, Eq. 2.3]:

$$\mathrm{SEFD} = \frac{2k_{\mathrm{B}}T_{\mathrm{sys}}}{\eta_{\mathrm{a}}A_{\mathrm{eff}}} \tag{2}$$

where k_{B} is the Boltzmann's constant, T_{sys} is the system's noise, η_{a} is the dipole efficiency (for the dipoles of SKA low) and A_{eff} is the effective area of each antenna[75]. For the ratio $\frac{A_{\mathrm{eff}}}{T_{\mathrm{sys}}}$ we have three different values 559([86]), 1000(SKA1 low[75]) and $4000\mathrm{m^2/K}$(SKA2 low[75]). Assuming the dipole efficiency is $\eta_{\mathrm{a}}=1$ we find three values for the SEFD:

$$\mathrm{SEFD}_1 = \frac{2\cdot1.38\times10^{-23}\mathrm{m^2kg\cdot s^{-2}K^{-1}}}{559\mathrm{m^2K^{-1}}} \tag{3}$$

$$\mathrm{SEFD}_1 = 4.9\mathrm{Jy} \tag{4}$$

$$\mathrm{SEFD}_2 = 2.8\mathrm{Jy} \tag{5}$$

$$\mathrm{SEFD}_3 = 0.7\mathrm{Jy} \tag{6}$$

5.2.2 Sensitivity of SKA1 low

SKA1 low can be used to detect 21cm absorption features of cold hydrogen clouds which are located in front of (in the line of sight) radio loud sources for redshifts greater than 6 and up to $z\sim15$[75].

Two necessary conditions for observations of neutral hydrogen clouds against high-z radio loud sources are the very existence of high redshift quasars and their detectability. The detectability of a quasar depends on its brightness and on the sensitivity of the detector. We can calculate the minimum flux density that an interferometer can detect [75, Eq. 3.1]:

$$\Delta\mathrm{S} = \frac{2\cdot k_{\mathrm{B}}T_{\mathrm{sys}}}{\mathrm{A_{eff}}\sqrt{\Delta\mathrm{v}t_{\mathrm{int}}}}\frac{\mathrm{S}}{\mathrm{N}} \tag{7}$$

where $\frac{\mathrm{S}}{\mathrm{N}}$ is the signal to noise ratio, $\Delta\mathrm{v}=10\mathrm{kHz}$[75] is the detector's bandwidth and t_{int} is the integration time. For a signal to noise ratio $\frac{\mathrm{S}}{\mathrm{N}}=3$ we can find the minimum detectable flux for a range of integration time for example between 100 and 1000 hours (for three different values of the ratio $\frac{\mathrm{A_{eff}}}{T_{\mathrm{sys}}}$):

$$\Delta\mathrm{S}_{1\mathrm{min}} = \frac{0.148}{\sqrt{t_{int}}}\mathrm{Jy} \tag{8}$$

$$\Delta\mathrm{S}_{2\mathrm{min}} = \frac{0.083}{\sqrt{t_{int}}}\mathrm{Jy} \tag{9}$$

$$\Delta\mathrm{S}_{3\mathrm{min}} = \frac{0.021}{\sqrt{t_{int}}}\mathrm{Jy} \tag{10}$$

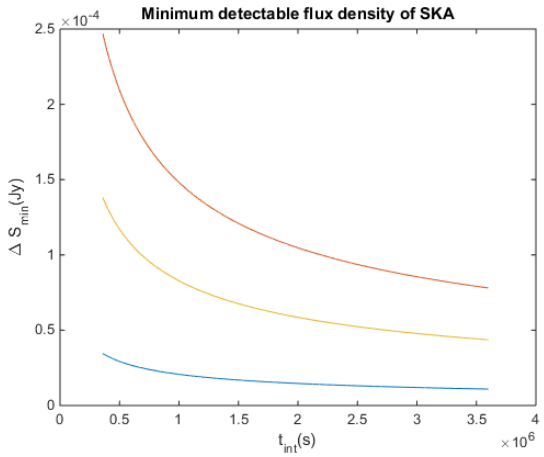

Figure 2: Minimum detectable flux density of SKA low with respect to integration time for $\mathrm{A_{eff}}/T_{\mathrm{sys}}=559\mathrm{m^2K^{-1}}$-red line, $\mathrm{A_{eff}}/T_{\mathrm{sys}}=1000\mathrm{m^2K^{-1}}$-yellow line and $\mathrm{A_{eff}}/T_{\mathrm{sys}}=4000\mathrm{m^2K^{-1}}$-blue line.

In Fig.2 we see how $\Delta\mathrm{S_{min}}$ changes with the integration time for the three values of the ratio $\mathrm{A_{eff}}/T_{\mathrm{sys}}$=559(red line), 1000(yellow line), $4000\mathrm{m^2K^{-1}}$(blue line).

5.3 Minimum detectable HI column density with SKA low

An estimation of the minimum column density that a cold hydrogen cloud must have in order to be detected requires a search for the possible range of the optical depths that the neutral hydrogen clouds could have for a specific wavelength.

5.3.1 Optical Depth

The optical depth of neutral hydrogen for $\lambda = 21$cm is given [75, Eq. 1.1]:

$$\tau_{21\mathrm{cm}}(z) = \frac{3}{32\pi}\frac{h_p c^3 A_{21\mathrm{cm}}}{k_b \nu_{21\mathrm{cm}}^2}\frac{x_{\mathrm{HI}} n_{\mathrm{H}}}{T_s(1+z)(dv_{\parallel}/dr_{\parallel})} \quad (11)$$

where h_p is the Planck constant, $A_{21\mathrm{cm}} = 2.85 \times 10^{-15}\mathrm{s}^{-1}$ is the Einstein coefficient for the transition that gives the particular absorption line, n_{H} is the neutral hydrogen number density, x_{HI} is the mean neutral hydrogen fraction, T_s is the spin temperature of the gas and $dv_{\parallel}/dr_{\parallel}$ is the gradient of the proper velocity along the line of sight[75]. There are several quantities in this equation which need further discussion, such as the spin temperature of the gas and the proper velocity along the line of sight[75].

The spin temperature T_s of a gas cloud is connected with its number density. The temperature that corresponds to the 21cm line is $T_* = 0.0681$K. This line is the result of the transition between the two hyperfine states of the ground level 1s of hydrogen. The energy difference of the two states is the result of the two different combinations of the nuclear and electron spins of 1/2(parallel or anti-parallel). Thus, the total spin at the ground state can be either 0(anti-parallel) or 1(parallel). In the case of parallel spins, the energy is greater. The energy difference of the transition between the two hyperfine states (21cm or 1420MHz line) is $\Delta E \sim 5.9 \times 10^{-6}$eV[78].

The spin temperature shows us the relative population of the two hyperfine states of the ground level. We assume that there are three mechanisms that contribute to the hyperfine transitions of a neutral hydrogen cloud: the CMB photons, collisions between atoms or electrons and Lyman(α) photons since more energetic radiation would ionize the cloud. Taking into consideration these contributions the spin temperature is [78, Eq.15]:

$$T_s = \frac{T_{\mathrm{CMB}} + y_C T_K + y_L T_L}{1 + y_C + y_L} \quad (12)$$

where y_C and y_L are the efficiencies for the collisions and Lyman photons respectively. In the case of a remote cloud we can ignore the photon contributions to spin temperature and Eq. 12 becomes:

$$T_s = \frac{T_{\mathrm{CMB}} + y_C T_K}{1 + y_C} \quad (13)$$

We investigate a cloud of HI, thus we assume $n_{\mathrm{e}}/n_{\mathrm{H}} < 10^{-3}$. If we combine the values for T_{K} and y_{C} where $y_{\mathrm{C}} = y_{\mathrm{H}} n_{\mathrm{H}} + y_e n_e$ which we take from the tables II and III of Field B.G 1958[78], we can calculate some approximate values for the spin temperature of a remote cloud of neutral hydrogen, for limit values of redshift 3 and 15 and gas temperatures 1,10,100 and 1000K:

$$T_{s1} = \frac{2.73(z+1) + 1200}{1201} \sim 1.01 - 1.04\mathrm{K} \quad (14)$$

$$T_{s10} = \frac{2.73(z+1) + 1900}{191} \sim 10.01 - 10.18\mathrm{K} \quad (15)$$

$$T_{s100} = \frac{2.73(z+1) + 3500}{36} \sim 97.53 - 98.44\mathrm{K} \quad (16)$$

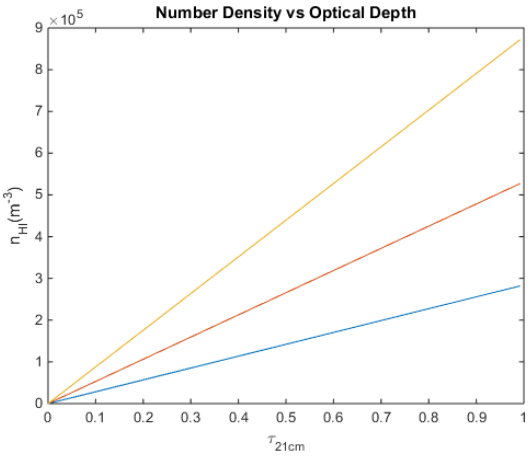

Figure 3: Number density of a HI cloud for redshifts 6(blue), 8(red) and 10(yellow) and $x_{\mathrm{HI}} = 1$.

$$T_{s1000} = \frac{2.73(z+1)+6700}{7.7} \sim 871.55 - 875.80\text{K} \quad (17)$$

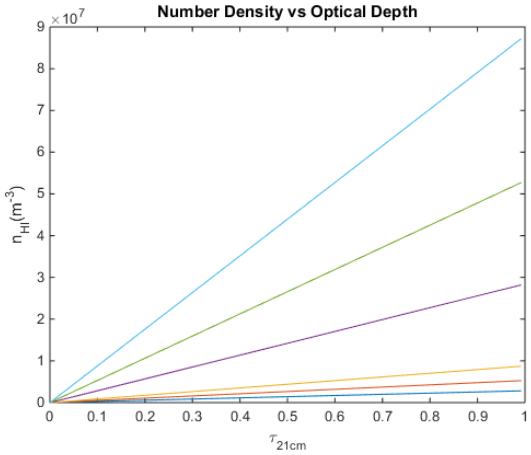

Figure 4: Number density vs optical depth of a HI cloud for $x_{\rm HI} = 0.1$ at redshifts 6(blue), 8(red) and 10(yellow) and for $x_{\rm HI} = 0.01$ at redshifts 6(purple), 8(green) and 10(light blue).

We notice that the redshift does not affect substantially the spin temperature. Now, we go back to the Eq. 11 to investigate the optical depth with respect to the number density of neutral hydrogen. We substitute all the constant quantities, the spin temperature with T_{s100}(Eq. 16) and we also assume that the neutral hydrogen fraction ($x_{\rm HI}$) takes three values: 1,0.1 and 0.01. Taking into consideration the optical depth range used for absorption in minihaloes by Furlanetto et al. 2006(Fig.5)[99], we estimate the neutral hydrogen number density for a chosen range of optical depth: $0.001 < \tau < 0.999$. Finally, to find the gradient of the proper velocity along the line of sight, we use Hubble's law and a Cosmology Calculator (http://www.astro.ucla.edu/~wright/CosmoCalc.html[79]). The results are given for three different values of redshift namely 6,8 and 10(Fig.3-Fig.4).

5.3.2 Column Density

Next, we calculate the column density from the number density (only for the case where $x_{\rm HI} = 1$), for MHs of mass $10^5 M_\odot$ and $10^6 M_\odot$ for a spherical and 2D disc distributions.

First we transform the number density to mass density. Then, for a mini halo mass of $M = 10^5 M_\odot$ and a spherical mass distribution we find the diameter of the cloud which shows us the maximum length of the cloud in the line of sight where we narrowed the optical depth range ($0.001 < \tau < 0.1$) to have a more detailed illustration of the cloud size (Fig.5). Afterwards, we calculate the column density by multiplying the diameter of the cloud with the number density(Fig.6).

We follow the same process for a cloud with a spherical mass distribution and a total mass of $M = 10^6 M_\odot$. The diameter vs the optical depth of this cloud can be seen in Fig.7 and its column density vs its optical depth in Fig.8.

We will find also how the column density of a cloud changes with respect to its optical depth when its mass is distributed on a disc of width 1 and 10 parsec for cloud masses $M = 10^5 M_\odot$ and $M = 10^6 M_\odot$ respectively. The diameter of a disc-shaped cloud vs its optical depth is shown in Fig.9 and Fig.11 for clouds of total mass of $M = 10^5 M_\odot$ and $M = 10^6 M_\odot$ respectively and the column density vs optical depth is shown in Fig 10 and Fig. 12. The results for the HI column density in all cases agree with the observational upper limit $\text{N(HI)}_{\rm max} = 10^{22}\text{cm}^{-2}$[93].

5.3.3 Minimum Flux Density

We will calculate the minimum flux density that a background source should have in order to be possible for absorption lines from a neutral hydrogen cloud to be detected with SKA1 low. We will use Eq.3.2 of Ciardi et al. 2015[75]:

$$S_{\rm min} = 4.37\text{mJy}\left(\frac{1000\text{hr}}{t_{\rm int}}\right)^{1/2}\left(\frac{0.01}{e^{-\tau_{\rm IGM}} - e^{-\tau}}\right) \quad (18)$$

where $\tau_{\rm IGM} = 0.066$[80] is the optical depth of the IGM. Fig. 13 shows us that quite strong sources

($S \gtrsim$ 6mJy) are required to detect absorption lines from a cloud.

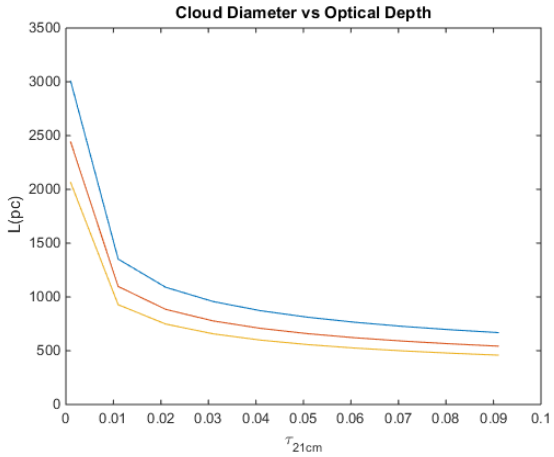

Figure 5: Diameter of a spherical cloud for redshifts 6(blue), 8(red) and 10(orange) and mass $M = 10^5 M_\odot$.

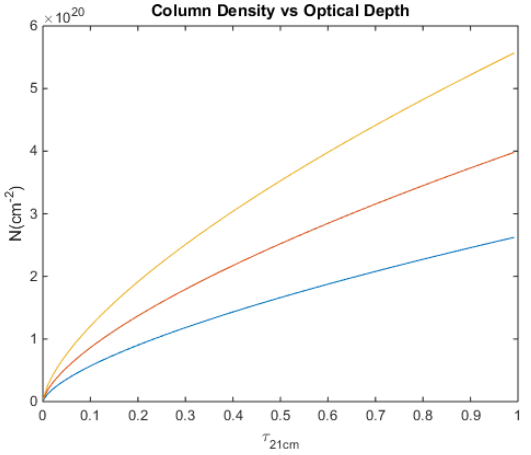

Figure 6: Column density vs optical depth of a spherical cloud for redshifts 6(blue), 8(red) and 10(orange) and mass $M = 10^5 M_\odot$.

5.3.4 Minimum Detectable Column Density

The next step is to find the minimum column density that a neutral hydrogen cloud should have in order to be detectable with SKA1 low. We consider two cases in which the spectral resolution of SKA1 low will be $\sim$ 10kHz and $\sim$ 1kHz in the frequency range 50-200MHz[81].

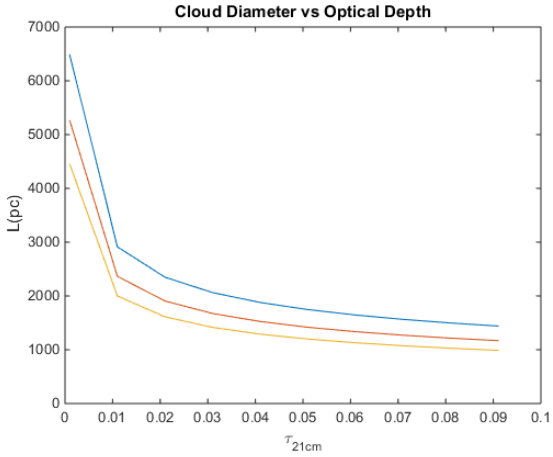

Figure 7: Diameter of a spherical cloud for redshifts 6(blue), 8(red) and 10(orange) and mass $M = 10^6 M_\odot$.

A) 10kHz

First we consider the case where the frequency resolution is 10kHz. Thus, this is the smallest frequency difference that the instrument can distinguish. The resolving power $R = \frac{f}{\Delta f}$ for this frequency range is between 5000 and 20000. The resolution expressed in velocity units ranges between 15 and 60 km/s and in wavelength units between 1.2mm-75μm.

Assuming the observed equivalent width of an absorption line at redshift 6.1 is equal to the resolution limit of SKA1 low we will use the relation for the linear part of the curve of growth to estimate the minimum column density of neutral hydrogen. Eq. 3.48 from [83] for an optical thin medium gives us:

$$\frac{W_\lambda}{\lambda} = 8.85 \times 10^{-13} N \lambda f \tag{19}$$

where N is the column density and f is the absorption oscillator strength ($f = 5.7786 \times 10^{-12}$[81]). The units of $N\lambda$ is cm^{-1}. We will replace W_λ with the intrinsic equivalent width and not the observed and we will replace the wavelength with the rest wavelength of the hyperfine hydrogen transition:

$$\mathrm{EW_{int1}} = \frac{\mathrm{EW_{obs}}}{1+z} = \frac{75\mu\mathrm{m}}{7.1} = 10.56\mu\mathrm{m} \tag{20}$$

$$\boxed{N_{\rm min1} \sim 0.47 \times 10^{18} {\rm cm}^{-2}} \quad (21)$$

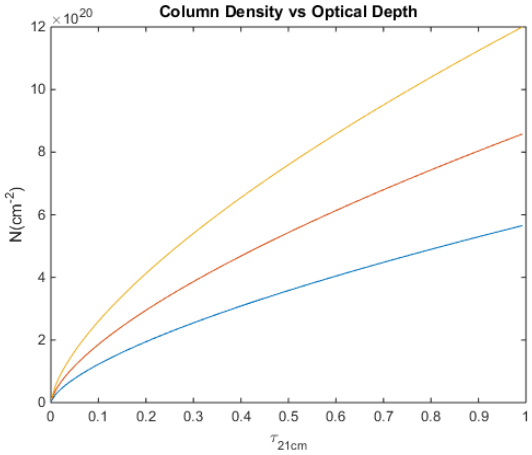

Figure 8: Column density vs optical depth of a spherical cloud for redshifts 6(blue), 8(red) and 10(orange) and mass $M = 10^6 M_\odot$.

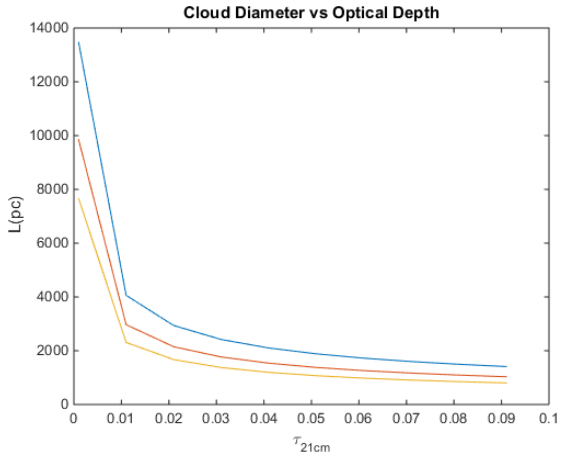

Figure 9: Diameter of a disc-shaped cloud vs optical depth for redshifts 6(blue), 8(red) and 10(orange) and mass $M = 10^5 M_\odot$.

We found the observed equivalent width from the transformation of frequency resolution (10kHz) to wavelength using the resolving power for 200MHz which corresponds to 21cm wavelength for redshift z=6.1 and then we found the desired column density from Eq.(19).

We repeat the above process for redshifts 8 and 10 to compare the results. For z=8 and an observed EW=120μm, the intrinsic EW and the column density are respectively:

$$\mathrm{EW}_{\rm int2} = \frac{\mathrm{EW}_{\rm obs}}{1+z} = \frac{120\mu{\rm m}}{9} = 13.3\mu{\rm m} \quad (22)$$

$$\boxed{N_{\rm min2} \sim 0.59 \times 10^{18} {\rm cm}^{-2}} \quad (23)$$

For z=10 and an observed EW=178μm, the intrinsic EW and the column density are:

$$\mathrm{EW}_{\rm int3} = \frac{\mathrm{EW}_{\rm obs}}{1+z} = \frac{178\mu{\rm m}}{11} = 16.2\mu{\rm m} \quad (24)$$

$$\boxed{N_{\rm min3} \sim 0.72 \times 10^{18} {\rm cm}^{-2}} \quad (25)$$

B) 1kHz

Now we consider the case where the frequency resolution is 1kHz which means that we assume that this is the smallest frequency difference that the instrument can distinguish in the frequency range 50-200MHz. From the resolving power we find the resolution expressed in velocity units 1.5km/s $< \Delta v <$ 6km/s and in wavelength units 0.12mm $< \Delta\lambda <$ 7.5μm.

We will use again Eq. (19) and (20) to find the intrinsic EW and minimum column density for redshifts z=6.1,8 and 10.

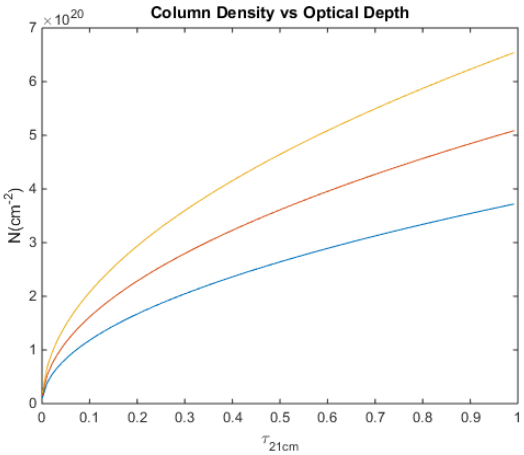

Figure 10: Column density of a disc-shaped cloud vs optical depth for redshifts 6(blue), 8(red) and 10(orange) and mass $M = 10^5 M_\odot$.

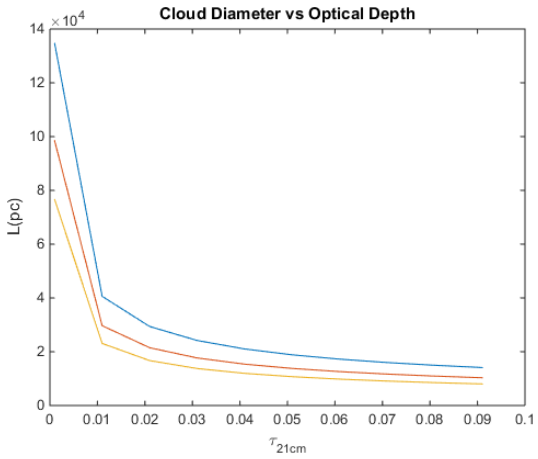

Figure 11: Diameter of a disc-shaped cloud vs optical depth for redshifts 6(blue), 8(red) and 10(orange) and mass $M = 10^6 M_\odot$.

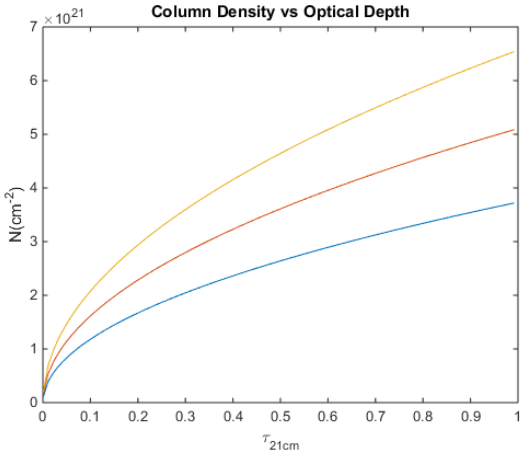

Figure 12: Column density of a disc-shaped cloud vs optical depth for redshifts 6(blue), 8(red) and 10(orange) and mass $M = 10^6 M_\odot$.

$$\mathrm{EW}_{\mathrm{int1}} = \frac{\mathrm{EW}_{\mathrm{obs}}}{1+z} = \frac{7.5\mu\mathrm{m}}{7.1} = 1.056\mu\mathrm{m} \qquad (26)$$

$$\boxed{N_{\mathrm{min1}} \sim 0.47 \times 10^{17}\mathrm{cm}^{-2}} \qquad (27)$$

For z=8 and an observed EW=12μm, the intrinsic EW and the column density are respectively:

$$\mathrm{EW}_{\mathrm{int2}} = \frac{\mathrm{EW}_{\mathrm{obs}}}{1+z} = \frac{12\mu\mathrm{m}}{9} = 1.33\mu\mathrm{m} \qquad (28)$$

$$\boxed{N_{\mathrm{min2}} \sim 0.59 \times 10^{17}\mathrm{cm}^{-2}} \qquad (29)$$

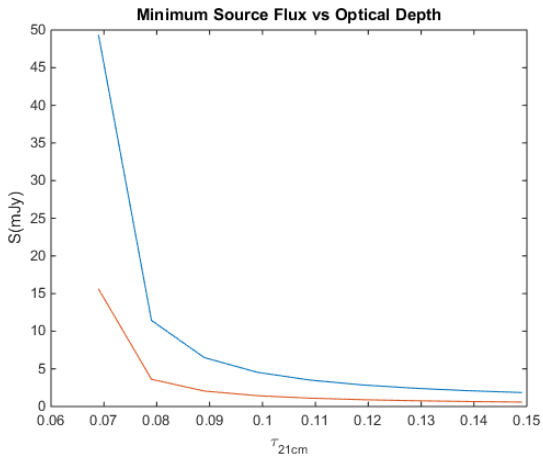

Figure 13: Minimum flux density of a background source so that the absorption lines of a neutral hydrogen cloud can be detectable for integration time of 1000hr(red) and 100hr (blue).

For z=10 and an observed EW=17.8μm, the intrinsic EW and the column density are:

$$\mathrm{EW}_{\mathrm{int3}} = \frac{\mathrm{EW}_{\mathrm{obs}}}{1+z} = \frac{17.8\mu\mathrm{m}}{11} = 1.62\mu\mathrm{m} \qquad (30)$$

$$\boxed{N_{\mathrm{min3}} \sim 0.72 \times 10^{17}\mathrm{cm}^{-2}} \qquad (31)$$

If we check the column density results in Fig. 6,8,10 and 12 for the corresponding optical depth we notice that $\tau << 1$. In Fig. 5 wee see that at redshift $z \sim 6$ and optical depth $\tau \sim 0.001$ the diameter of a neutral hydrogen cloud of mass $\mathrm{M} = 10^5 \mathrm{M}_\odot$ is approximately 3kpc, while the size of a gas cloud of mass $\mathrm{M} = 10^6 \mathrm{M}_\odot$ at redshift $z \sim 6$ and with optical depth $\tau \sim 0.001$ is approximately 6.5kpc.

6 Spectroscopy

Spectrographs are divided in two types depending on the optical device that is used to split the incoming light to its component wavelengths so that it can be analysed. Prism-based spectrographs are based on differential diffraction whereas diffraction gratings spectrographs are based on interference and diffraction of waves[70]. Spectrographs that are used in astronomy usually work with diffraction gratings rather than prisms because they are more efficient[67]. A diagram of a slit spectrograph with diffraction grating can be seen in Fig.14.

After the incoming light passes through the slit, it is made parallel by a collimator and then it is reflected and dispersed into its component wavelengths. Finally a camera mirror focuses the light to a detector, usually a Charged-Coupled Device (CCD) and from there the spectrum is recorded in a computer for further analysis[68].

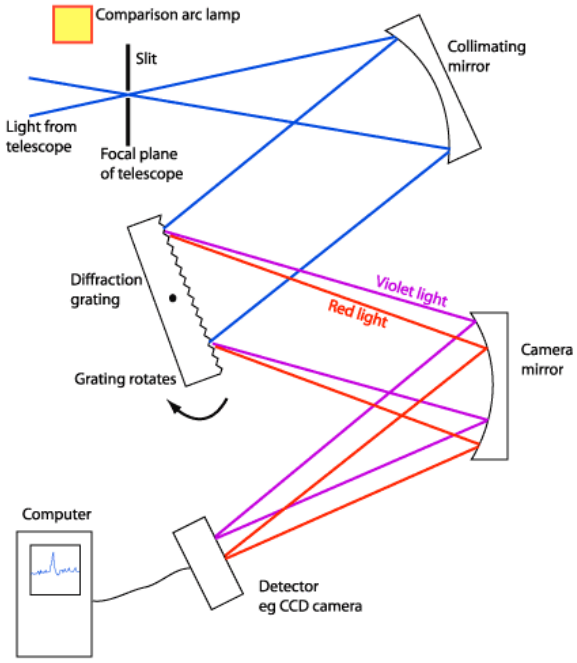

Figure 14: Slit Spectrograph
image credit[67]

6.1 Diffraction Gratings

Diffraction grating is a structure of parallel and narrow-spaced slits which is used to disperse the incoming light. Often, the diffraction gratings are inclined to the incident light beam. There are two types of gratings: transmission and reflection gratings. Transmission gratings are formed on a thin metal film deposited on a substrate. The areas which do not have any metal in them act as transmission slits. A typical example of a transmission diffraction grating has thousand lines per millimetre[70].

On the other hand, in Fig. 15, the optical paths of incident light rays on reflection gratings can be seen.

The spectral resolution of a spectrograph is[70, Eq. 4.20]:

$$W = \frac{\lambda}{Nm} \tag{32}$$

where N is the number of grooves and m is the spectral order. Thus, the resolving power which is given by the equation [70, Eq. 4.21]:

$$R = \frac{\lambda}{W} \tag{33}$$

becomes:

$$R = Nm \tag{34}$$

To find the angular positions of intensity maxima we use the grating equation [70, Eq. 4.24]:

$$\theta = \sin^{-1}\left[\left(\frac{m\lambda}{d}\right) - \sin i\right] \tag{35}$$

where i is the inclination of the grating with respect to the incoming light and d is the distance between the slits.

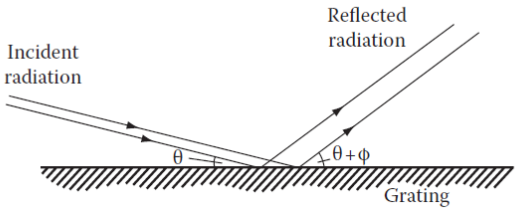

Figure 15: Grazing incidence reflection grating
image credit[70]

6.2 Fibre-fed Spectrographs

Fibre-fed spectrographs is another type of spectrographs that has been developed the last decades[69]. In contrast to the plain slit spectrographs the fibre-fed ones can detect several objects that there are inside the FoV instead of just one (Multi-object spectroscopy). Optical fibres are placed on the focal surface of the telescope. The incoming light of each object illuminates one fibre. The fibres then are led to the entrance slit of the spectrograph. Finally, the spectra of the objects appeared on the CCD detectors. The advantage of these spectrographs is that they can record spectra from numerous targets simultaneously, however the fibres must be re-arranged every time the FoV changes. The number of fibres sets the limit on the number of the object targets the spectra of which can be simultaneously obtained (multiplex gain)[68].

6.3 The European Extremely Large Telescope (E-ELT)

The E-ELT will be the largest optical and near-infrared telescope with a 39-meter aperture and it will provide pictures sixteen times sharper than Hubble Space Telescope due to its adaptive optics systems. The first construction phase (out of two) has already started on the mountain Cerro Armazones, in Atacama Desert in Chile[55][56]. The telescope is supported by an altitude azimuth mount, the weight of which is 2800 tonnes[57]. Adaptive optics (AO) are included in the telescope, thus the telescope consists of five mirrors: a folded three-mirror anastigmat and two folding mirrors (for AO), creating a 10-arcmin Field of View (FoV). The telescope has two Nasmyth platforms, along the elevation axis of the telescope, which can support additional instruments[57][58].

The primary mirror (M1) is a segmented 39-meter elliptical mirror with central obstruction diameter of 11.1 meters. It consists of 798 hexagonal segments of maximum dimension 1.45 meters. The secondary mirror (M2) is a 4.2-meter convex mirror that reflects the light through a hole in the fourth mirror (M4) to the tertiary mirror (M3) which is an aspheric concave 3.8-meter mirror. The optical design can be seen in Fig 16. M4 is an adaptive optics flat mirror of size 2380x2340mm which is supported by 8000 actuators and is inclined by 7.75° with respect to the beam direction. The fifth mirror (M5) which is the second adaptive optics mirror of size 2.6m by 2.1m, sends the beam to the Nasmyth foci. An additional coudé focus is included in the telescope to accomplish the requirements for a narrow field high resolution spectrograph[58][59].

The main structure that supports the telescope is an altitude azimuth mount which includes two parts: the Azimuth and the Altitude structure. The former supports the scientific instruments and the Nasmyth platforms while the latter supports the telescope optics[60].

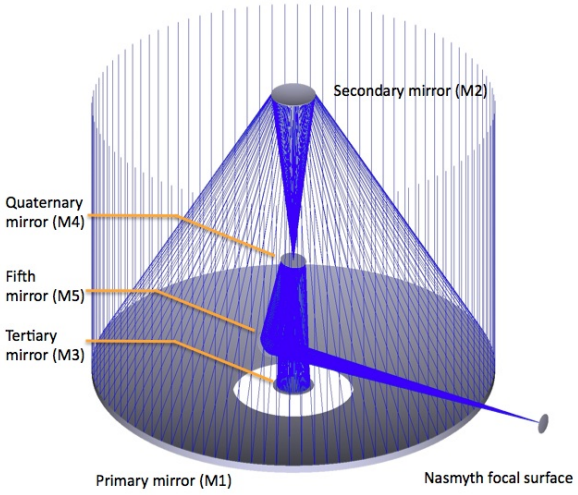

Figure 16: Optical design of E-ELT
image credit[55]

The instruments that are planned for the E-ELT are a diffraction-limited near-infrared imager (ELT-CAM), a single-field near-infrared wide-band integral field spectrograph (ELT-IFU), a mid-infrared imager and spectrometer (ELT-MIDIR), a high resolution spectrometer (ELT-HIRES), a multi-object spectrometer (ELT-MOS), a planetary camera and spectrograph (ELT-PCS) and an additional instrument which has not yet been specified[61].

The E-ELT will probe black holes, stars, galaxy formation, it will search for exoplanets as well as for

the first stars and galaxies and finally it will shed light to some unclear matters of fundamental physics such as dark matter and dark energy[62]. With the existing telescopes we can observe the universe back to redshift 6. So far, galaxy formation and evolution studies for redshift larger than one are possible only for the brightest and the most massive galaxies. However, E-ELT will observe the universe for redshifts greater than six and closer to the dark ages and lead to a deeper understanding of galaxy evolution[62].

6.4 Requirements of HiReS

The High Resolution Spectrograph on the E-ELT will be used to search the Pop III SN signatures in the IGM and the ISM. To achieve this goal it needs spectral resolution $R > 50,000$[53]. HiReS will be able to search for the chemical enrichment from Pop III stars in individual second generation stars in Milky Way and in galaxies of the Local Group. For example, it will search for indicators of chemical enrichment that are expected if the stars (SG) are only polluted by Pop III explosions (not from SNII, SNIa, Novae, AGB stars). Stellar abundances of FeI and FeII, of α elements as well as s- and r-elements would be investigated[54].

The requirements for observations of individual stars in our Galaxy and in the closest to the Milky Way galaxies in order to investigate whether or not they are second generation stars are shown in Table 7[54].

Table 7: HiReS requiremetns for Spectroscopy of metal poor and extremely metal poor stars[54].

Spectral Resolution	50,000 (goal: 100,000)
Wavelength Range	0.38-0.8 μm
Spatial resolution	Seeing limited
Entrance aperture	1
Calibration	Wavelength:$\sim$ 100m/s
Sensitivity	S/N = 70 for 21mag in 3h

On the other hand, if we want to investigate gas clouds in IGM, where the signs of the death of the first stars might be, we search for gas clouds that happen to be at the line of sight in front of quasars and thus we detect absorption lines. E-ELT will search for Very Metal Poor (VMP) DLA systems (carbon enhanced or not) and it will be able to detect weak lines of Fe-peak elements, and thus their ratios (Ti/Fe, Cr/Fe, Co/Fe, Ni/Fe, Zn/Fe) could be calculated. What is more, E-ELT will search for the signatures of Pop III stars at higher redshift DLAs than it is possible at present and also look for fainter quasars. That means high resolution spectroscopy is needed ($R \sim 100,000$) for the detection of narrow (few km/s) and weak absorption lines. Besides the search for the nucleosynthetic yields in VMP DLAs, HiReS will look for low ionization metal absorbers in gas clouds in the IGM at higher redshifts ($z > 6$). However, to achieve at the same time high continuum S/N for faint quasars at high redshifts ($z > 6$) the spectral resolution might need to be lower $R \sim 50,000$[54]. The HiReS requirements for IGM observations are presented in Table 8.

Table 8: HiReS requirements for detecting metal spectral lines in the IGM[54].

Spectral Resolution	50,000 (goal: 100,000)
Wavelength Range	0.6-1.8 μm (goal:0.4-2.4 μm)
Spatial resolution	Seeing limited
Entrance Aperture	1
Calibration	Sky subtraction:yes
Sensitivity	S/N = 50 for 21mag in 5h

7 Observations with HiReS

7.1 Low ionization metal absorbers

The optical depth (τ) for an absorption line at the centre of the line is given by ([89, Eq 9.8]):

$$\tau = \frac{\sqrt{\pi} e^2 N f \lambda}{m_e c b} \tag{36}$$

where N is the column density of the element we are interested in, f is the oscillator strength, and b is the broadening parameter (assuming Doppler broadening). If we substitute, besides the known constant values, the oscillator strength for the transition that results in wavelength $\lambda = 1302.17$Å (OI), $f = 5.2 \times 10^{-2}$[90] and the broadening factor for $T = 100$K, $b = 0.32\text{kms}^{-1}$[89, Eq. 6.34] we have:

$$\tau = 3.17 \times 10^{-13} \cdot N \tag{37}$$

where N is measured in cm^{-2}. We found how the optical depth depends on the column density for OIλ1302. In Fig. 17 we see how the column density (OIλ1302) changes with optical depth for τ in the range $0.001 < \tau < 4.999$.

Next, we want to find the minimum detectable column density of OI. We will estimate the N_{OI} for z=6. The wavelength $\lambda_6 = 911.4$nm is well in the range of HiReS as we can check in Table 8.

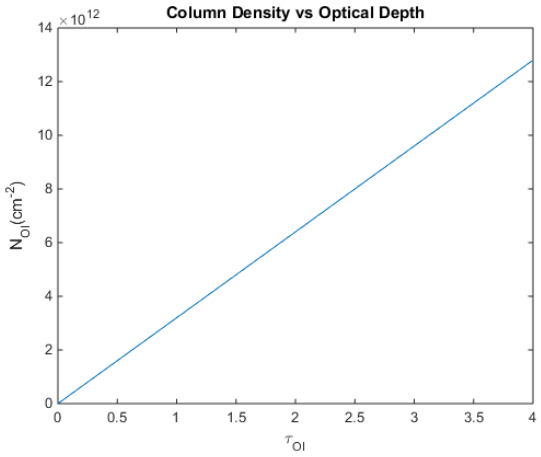

Figure 17: Column Density vs Optical depth of OI

Since we are interested only in the minimum detectable column density we will use the linear part of the equations for the curve of growth which describes the optically thin case. We will use again Eq. 19 which shows us the column density with respect to the equivalent width of an absorption line [89, Eq. 9.15] :

$$N = 1.13 \times 10^{12} \frac{W}{\lambda} \frac{1}{f\lambda} \mathrm{cm}^{-1} \tag{38}$$

In the Table 7 we can see that the initial spectral resolution (resolving power) of HiReS is 50000 with the goal being 100000. We will calculate the minimum N(OI) for two different cases. We will assume that the wavelength resolution of HiReS is the equivalent width of the absorption line OIλ1302 and then we will calculate the hypothetical intrinsic equivalent width as we did also for SKA.

First, for resolution 50000 and redshift $z = 6$ we have:

$$\boxed{N = 3.34 \times 10^{13} \mathrm{cm}^{-2}} \tag{39}$$

This result is similar to the column densities that were measured with HIRES on Keck and MIKE on Magellan for low ionization absorption systems at redshifts $\sim$ 6 where the lowest value for $\log \mathrm{N_{OI}}$ is $\sim$ 13.5[87].

Finally, for resolution 100000 and redshift $z = 6$ we have:

$$\boxed{N = 1.67 \times 10^{13} \mathrm{cm}^{-2}} \tag{40}$$

The same gas cloud can be observed by both SKA and E-ELT. SKA could measure the neutral hydrogen column density and HiReS could measure the column density of the metal in which we are interested from its absorption line. For example, we can find the radius R of a spherical cloud of mass $10^6 \mathrm{M}_\odot$ and a column density $\mathrm{N_{HI}} = 0.47 \times 10^{18} \mathrm{cm}^{-2}$ (minimum detectable HI column density with SKA) , if we assume a hydrogen fraction of 0.75:

$$N = nLx = 2nRx = \frac{2Rx\rho}{m_\mathrm{H}} = \frac{2RM}{\frac{4}{3} m_\mathrm{H} \pi R^3} \tag{41}$$

$$R = 9.75\mathrm{kpc} \tag{42}$$

where n is the number density, L is the diameter of the cloud, x is the hydrogen fraction, ρ is the hydrogen mass density of the cloud, m_H is the mass of a hydrogen atom and M is the total mass of the cloud. We can observe the same cloud with HIRES to measure the oxygen abundance. For the same total mass and size, if we substitute in Eq. 41 the minimum OI column density we found (Eq. 39), and the mass of an oxygen atom m_O instead of hydrogen, we find the fraction of oxygen in the cloud which is $x_\mathrm{O} = 0.085\%$.

Now, we will find the minimum abundance of OI using the neutral hydrogen and oxygen column densities we have already calculated. The minimum OI and HI column densities are respectively (Eq. 38, Eq. 21): $\mathrm{N(OI)} = 3.34 \times 10^{13} \mathrm{cm}^{-2}$, $\mathrm{N(HI)} \sim 0.5 \times 10^{18} \mathrm{cm}^{-2}$.

Thus, the minimum detectable OI abundance (from OIλ1302 line) is:

$$O/H = \log_{10}\left(\frac{N(OI)}{N(HI)}\right) = \log_{10}(6.68 \times 10^{-5}) \quad (43)$$

$$O/H \approx -4.2 \quad (44)$$

In addition, the oxygen abundance with respect to the solar is:

$$[O/H] = \log_{10}\left(\frac{N(OI)}{N(HI)}\right) - \log_{10}\left(\frac{N(OI)}{N(HI)}\right)_{\odot} \quad (45)$$

After we substitute the solar neutral oxygen abundance: 8.69 ± 0.05 [91] Eq. 43 becomes:

$$[O/H] = \log_{10}\left(\frac{N(OI)}{N(HI)}\right) - 8.69 + 12 \quad (46)$$

$$[O/H] = -0.95 \quad (47)$$

As we can see, the minimum oxygen abundance that HIRES will be able to detect at the SKA detection threshold is ~ -1 which means 10% of the solar oxygen abundance. This value may not be low enough especially for metals such as iron, for which the abundance is expected to be $[Fe/H] < -1$, however for oxygen it may be adequately low, considering that the oxygen abundance is expected to be higher than iron.

7.2 CEMP DLAs

The signatures of Pop III stars may be found, as we have already seen, in CEMP stars, in the atmospheres of which we detect high abundances of carbon and low metallicities. Therefore, if it is possible for SG stars to maintain Pop III signatures (high CNO to Fe ratios) in their atmospheres, these signs of the first stars should be visible also in gas systems that already hosted Pop III stars (assuming that the high abundance of carbon relative to iron comes in fact from Pop III SNe and not another source). Although it is difficult to detect CEMP DLAs, because VMP DLAS are rare and the measurement of their carbon abundance is quite difficult due to the saturation of the corresponding absorption lines[38], Cooke et al. 2011a[38] have discovered a VMP ([Fe/H<-2]) DLA at redshift z=2.34 that shows carbon enhancement similar to CEMP stars[38].

The abundances of this DLA were [Fe/H]=-3.04, [O/H]=-2.28, [C/O]=+0.77 and [C/Fe]=+1.53. An odd-even effect was observed also making this object a serious candidate for hosting Pop III stars. However, the abundances are consistent with the yields of a star in a mass range of $20 - 50 M_{\odot}$, which exploded as CCSN and not PISN[38].

Cooke et al. 2012[32] searched among already discovered VMP DLAs to detect a possible carbon enhancement. They chose a DLA at redshift z=3.0675, discovered by Penprase et al. 2010[97]. This DLA showed abundances [O/H]=-3.08, [C/O]=+0.44 and [C/Fe]=+0.8[32][97]. They performed high resolution follow up observations and found [Fe/H]=-2.84, [O/H]=-2.22 and [C/O]~0 pointing out the importance of high resolution spectroscopy[32]. Carbon and oxygen were enhanced with respect to iron. However, they showed that it is not possible to distinguish if these signatures come from Pop III or Pop II CCSNe[32].

7.3 PISN signatures

When high redshift damped Lyman alpha systems are observed, the odd-even effect that is caused by PISNe can be detected. The spectral signatures of the explosions depend not only on the mass and the released energy but also on the progenitor size and structure, the envelope and its structure and finally on the absorption that might happen by the IGM and ISM[73].

A gas cloud of mass $M = 4 \times 10^8 M_{\odot}$ can be enriched up to $[Fe/H] = -4$ by just one event of PISN[6]. Searching in VMP DLAs for the abundances of metals and the expected odd-even effect and comparing to the values that the models have shown for the nucleosynthesis of PISNe should be a really helpful step towards the confirmation of Pop III signatures. For gas clouds at redshifts $z \geq 6$, observations and measurements in radio frequencies will show us the hydrogen densities, thus it will be feasible to measure the abundances of some metals in order to understand weather or not a gas cloud/halo

in the IGM hosted Pop III stars but there has not been any star formation in it since their death.

8 Conclusion

We have seen how the death of the first stars which were formed by pristine gas, played an important role in the chemical enrichment and evolution of the early IGM. Searching for the signs of their existence means that we should search either for individual metal poor stars which may have conserve some signatures in their atmospheres or for metal poor gas clouds which may also still bear the nucleosynthetic yields of them.

Very metal poor stars which could be second generation stars can be found in the halo or the bulge of the Milky Way or in other (dwarf) galaxies of the local group. A special characteristic that it is believed to be connected to the death of Pop III stars is the high abundance of carbon in comparison to iron in these stars' atmospheres (CEMP stars).

If we want to search at higher redshifts though, we should look for metal poor gas clouds, either DLAs at redshifts up to $z \sim 5-6$ or neutral hydrogen gas clouds to find low ionization metal absorbers for redshifts $z \geq 6$. Assuming that gas clouds that hosted Pop III stars and have not been contaminated yet by Pop II SNe exist and are detectable, we could find gas that is carbon enhanced but also shows an odd-even effect as the models of PISNe predict. The expected abundances of PISNe are known, thus, any observations can be compared with the theoretical values. The difficulty of measuring abundances for redshifts higher than six is the measurement of the hydrogen column density. However, high resolution observations in radio-frequencies e.g. with SKA, could be proved helpful.

New high resolution telescopes such as E-ELT and SKA will help unravelling some of the unanswered yet questions about the chemical enrichment of the early universe and death of the first stars.

REFERENCES

1. Gray O. Richard, Corbally J. Christopher, Burgasser J. Adam, Stellar Spectral Classification, 2009, Princeton University Press

2. Turk J.Matthew, Abel Tom, O'Shea Brian, 2009, Science Vol. 325, no. 5940, pp 601-605

3. Heger A., Woosley S.E., 2010 ApJ 724:341-373

4. Ji A. P., Frebel A., Bromm V. 2015 MNRAS arXiv:1508.06137v1

5. Norris John E. et al. 2013 ApJ 762:28 (19pp) doi:10.1088/0004-637X/762/1/28

6. Heger A., Woosley S.E. 2002 ApJ 567 : 532-543

7. Joggerst C. C., Almgren A., Bell J., Heger A., Whalen D., Woosley S. E., 2010, ApJ, 709, 11

8. Tegmark M., Silk J., Rees M. J., Blanchard A., Abel T., Palla F., 1997, ApJ, 474, 1

9. Oh S.P. & Haiman Z. 2002 ApJ 569:558-572

10. Abel T., Bryan G. L., Norman M. L., 2002, Science, 295, 93

11. Greif T. H., Johnson J. L., Bromm V., Klessen R. S., 2007, ApJ, 670, 1

12. Clark P. C., Glover S. C. O., Klessen R. S., 2008, ApJ, 672, 757

13. Beers T. C., Christlieb N., 2005, ARA&A, 43, 531

14. Karlsson T., Johnson J. L., Bromm V., 2008, ApJ, 679, 6

15. Johnson J. L., Greif T. H., Bromm V., 2008, MNRAS, 388, 26

16. Ritter J. S., Safranek-Shrader C., Gnat O., Milosavljevic M., Bromm V., 2012, ApJ, 761, 56

17. Jeon M., Pawlik A. H., Bromm V., Milosavljevic M., 2014, MNRAS, 444, 3288

18. Couchman H. M. P., Rees M. J., 1986, MNRAS, 221, 53

19. Greif T. H., Johnson J. L., Klessen R. S., Bromm V., 2008, MNRAS, 387, 1021

20. Nomoto K., Tominaga N., Umeda H., Kobayashi C., Maeda K., 2006, Nuclear Physics A, 777, 424

21. Iwamoto N., Umeda H., Tominaga N., Nomoto K., Maeda K., 2005, Science, 309, 451

22. Hirschi R., 2007, A&A, 461, 571

23. Nomoto K., Kobayashi C., Tominaga N., 2013, ARA& A, 51, 457

24. Tumlinson J., 2006, ApJ, 641, 1

25. Norris J. E., et al., 2013, ApJ, 762, 28

26. Umeda H., Nomoto K., 2002, ApJ, 565, 385

27. Meynet G., Ekström S., Maeder A., 2006, A&A, 447, 623

28. Aoki W., Beers T. C., Christlieb N., Norris J. E., Ryan S. G., Tsangarides S., 2007, ApJ, 655, 492

29. Jeon M., Bromm V., Pawlik A. H., Milosavljevic M., 2015, MNRAS, (arXiv:1501.01002)

30. Frebel A., Bromm V., 2012, ApJ, 759, 115

31. Frebel A., Simon J. D., Kirby E. N., 2014, ApJ, 786, 74

32. Cooke Ryan, Pettini Max, Murphy T. Michael, 2012, MNRAS 425, 347–354, doi:10.1111/j.1365-2966.2012.21470.x

33. Mateo M. L., 1998, ARA&A, 36, 435

34. Weisz D. R., et al., 2011, ApJ, 739, 5

35. Wolfe A. M., Turnshek D. A., Smith H. E., Cohen R. D., 1986, ApJS, 61, 249

36. Pettini M., King D. L., Smith L. J., Hunstead R. W., 1997, ApJ, 478, 536

37. Ellison S. L., Prochaska J. X., Hennawi J., Lopez S., Usher C., Wolfe A. M., Russell D. M., Benn C. R., 2010, MNRAS, 406, 1435

38. Cooke R., Pettini M., Steidel C. C., Rudie G. C., Jorgenson R. A., 2011a, MNRAS, 412, 1047

39. Cooke J. Ryan, Pettini Max, Jorgenson A. Regina, 2015, ApJ 800:12 (17pp), doi:10.1088/0004-637X/800/1/12

40. Vladilo G., Abate C., Yin J., Cescutti G., Matteucci F., 2011, A&A, 530, A33

41. Venn K. A., Irwin M., Shetrone M. D., Tout C. A., Hill V., Tolstoy E., 2004, AJ, 128, 1177

42. Sluder A. et al. 2015 MNRAS 456, 2

43. McKee, C. F., & Tan, J. C. 2008, ApJ, 681, 771

44. Tumlinson, J. 2006, ApJ, 641, 1

45. Stacy, A., Bromm, V., & Loeb, A. 2011, MNRAS, 413, 543

46. Schaerer, D. 2002, A&A, 382, 28

47. Yong, D., Norris, J. E., Bessell, M. S., et al. 2013, ApJ, 762, 27

48. Ritter J. S., Sluder A., Safranek-Shrader C., Milosavljevic M., Bromm V., 2015, MNRAS, 451, 1190
arXiv:1408.0319v2

49. Arnett, W. D., & Meakin, C. 2011, ApJ, 733, 78

50. Talbot, R. J., Jr., & Arnett, W. D. 1973, ApJ, 186, 51

51. Cooke, R., & Madau, P. 2014, arXiv:1405.7369

52. Fumagalli M. et al. 2011 arXiv:1111.2334v1

53. Maiolino R. et al., *A Community Science Case for E-ELT HiReS*

54. Liske Jochen, Spyromilio J., Tamai R., 2014, E-ELT Programme, Top Level Requirements for E-ELT HIRES, ESO-204697 Version 1

55. URL: www.eso.org/sci/facilities/eelt

56. URL: www.eso.org/public/news/eso1440

57. URL: www.eso.org/sci/facilities/eelt/telescope /index.html

58. URL: www.eso.org/sci/facilities/eelt/telescope /design

59. URL: www.eso.org/sci/facilities/eelt/telescope /mirrors

60. URL: www.eso.org/sci/facilities/eelt/telescope/ mstructure

61. URL: www.eso.org/sci/facilities/eelt/ instrumentation

62. URL: www.eso.org/sci/facilities/eelt/science/ doc/eelt_sciencecase

63. URL: www.eso.org/sci/facilities/eelt/docs/ E-ELT-Construction-Proposal-INS_Chapter

64. URL: www.iac.es/proyecto/codex

65. URL: www.iac.es/proyecto/codex/ pages/laser-comb.php

66. Pasquini Luca et al., *CODEX: The high resolution visual spectrograph for the E-ELT*, doi:10.1117/12.787936

67. URL: www.atnf.csiro.au/outreach/education/ senior/astrophysics/spectrographs.html

68. URL: www.starlink.rl.ac.uk/docs/sc14.htx/ sc14pa2.html#x3-110005

69. URL: www.starlink.rl.ac.uk/ docs.sc14.htx/sc14pa1.html

70. Kitchin Christopher R. *Astrophysical Techniques*, CRC PRess, Taylor & Francis Group 2014

71. Seiradakis H. John, *Εισαγωγή στη Ραδιοαστρονομία*, ΠΛΑΝΗΤΑΡΙΟ Θεσσαλονίκης, 2009

72. URL: https://www.skatelescope.org

73. Whalen J. Daniel et al., 2013, arXiv:1211.4979v4

74. Cordes James, Campbell Don, Lo Fred, 2009, *The Square Kilometer Array* Project Description for Astro2010

75. Ciardi B., Inoue S., Mack J.K., Xu Y., Bernardi G. 2015 arXiv:1501.04425v1

76. Schilizzi T.R. et al., 2007, MEMO100 *Preliminary Specifications for the Square Kilometre Array*

77. Field B.G., 1959, ApJ,..129..536F

78. Field B.G., 1958, Proceedings of the IRE

79. URL: http://www.astro.ucla.edu/ wright/ CosmoCalc.html, Cosmology Calculator

80. Planck Collaboration: P. A. R. Ade et al. 2015, arXiv:1502.01589v2

81. Minh Huynh, (International Center for Radio Astronomy Research/Uni of Western Australia and SKA Program Development Office),

Deputy International SKA Project Scientist, Key Science and Technical Requirements for SKA-low

82. Wiese L.W., Fuhr R.J., 2009, J. Phys. Chem. Ref. Data, Vol. 38, No. 3

83. Spitzer Lyman Jr., Physical Processes in the Interstellar Medium, Princeton University Observatory, 1978/1998 by John Wiley & Sons, Inc.

84. Price C.D., Hickish J., Sinclair D., Jones E.M., 2013, MEMO150, Optimal Partitioning of SKA low antenna elements

85. Cornwell T., McPherson A., Diamond P., Braun R., 2014, SKA Phase 1 Science (Level 0) Requirements Specification, SKA-OFF.SE.ARC-SKO-SCI-001_1

86. Dewdney P. et al., Stevenson J. T., McPherson M. A., Turner W., Braun Robert, Santander-Vela Juande, Waterson Mark, Tan G-H, 2015, SKA1 System BaselineV2 Description, Doc.No: SKA-TEL-SKO-0000308

87. Becker D.G., Sargent L.W.W., Rauch M., Calverley P.A., 2011, ApJ, 753:93(15pp)

88. Becker D.G., Bolton S.B., Lidz A., 2015, Publications of th Astronomical Society of Australia, Vol. 32, e045
doi:10.1017/pasa.2015.45

89. Drain T. Bruce, Physics of the Interstellar and Intergalactic Medium, 2011, Princeton University Press

90. Wiese L.W., Fuhr R.J., Deters M.T., 1996, Journal of Physical and Chemical Reference Data, Monograph No.7

91. Asplund M., Grevesse N., Sauval Jacques A., Scott P., 2009, ARAA Vol.47:481-522

92. Encyclopaedia of Astronomy and Astrophysics, Lyman Alpha Forest, 2001, Nature Publishing Group

93. Schaye Joop, 2001, ApJ 562, L95, doi: 10.1086/338106, arXiv:astro-ph/0109280

94. Wolfe M. Arthur, Gawiser Eric, Prochaska X. Jason, 2005, Annual Reviews of Astronomy & Astrophysics 43:861-918,
doi: 10.1146/annurev.astro.42.053102.133950, arXiv:astro-ph/0509481

95. Schaye J., Aguirre A., Kim Tae-Sun, Theuns T., Rauch M., Sargent L.W.W., 2003, ApJ 596:768–796

96. Simcoe A.R., L.W.W., l Rauch M., 2004, ApJ 606:92–115

97. Penprase E. Bryan et al., 2010, ApJ 721:1–25
doi:10.1088/0004-637X/721/1/1

98. Visbal Eli, Haiman Zoltan, Bryan L. Greg, 2015, MNRAS 453, 4456–4466, doi: 10.1093/mnras/stv1941

99. Furlanetto R. Steven, 2006, MNRAS, 370, 1867-1875, doi: 10.1111/j.1365-2966.2006.10603.x